Available online at www.sciencedirect.com
SCIENCE DIRECT®
ELSEVIER
Icarus 165 (2003) 414–427
ICARUS
www.elsevier.com/locate/icarus

Planetary regolith surface analogs: optimized determination of Hapke parameters using multi-angular spectro-imaging laboratory data

Aurélien M. Cord,* Patrick C. Pinet, Yves Daydou, and Serge D. Chevrel

Laboratoire de Dynamique Terrestre et Planétaire (UMR5562/CNRS/Université Paul Sabatier), Groupe de Recherche de Géodésie Spatiale, Observatoire Midi-Pyrénées, Toulouse, France

Received 16 July 2002; revised 17 June 2003

Abstract

This work presents a method for a determination of the global set of parameters involved in Hapke's model for planetary surface analogs when dealing with a set of angular conditions representative of the usual range of observation in planetary exploration for spaceborne optical instruments. The present approach is founded on a genetic algorithm: the whole set of Hapke parameters is treated simultaneously without any a priori assumptions. It limits the risk of meeting a local extreme, and the stability and repeatability of the determination are improved. Moreover, it requires less computational time than a Monte Carlo routine. As a demonstration, using multi-angular measurements acquired by a new laboratory wide-field multispectral imaging facility, parameter values for various grain sizes and material compositions of planetary regolith surface analogs are derived and their potential wavelength dependence is studied. The results, coherent with the literature, validate all the steps in our methodology. We focus our interest in the understanding of the physical meaning of Hapke's parameters, in particular of the parameter θ of the shadowing function for macroscopic roughness. It appears that the features smaller than the centimeter scale contribute predominantly to the photometric effect related to the rocky aspect of planetary soil surfaces. The parameter θ may thus be mainly considered as an integral of the roughness properties in the submillimetric-centimetric range. Indeed, the most representative case for describing natural regolith surface lies in texture classes in the millimeter range, not involving necessarily a high macroscopic roughness with large surface slopes at hundreds of meters scale. These findings strengthen the case that θ depends on both the grain size and the material geological properties.

Keywords: Hapke's model; Experimental measurements; Reflectance spectroscopy; Function for macroscopic roughness; Genetic algorithm

1. Introduction

Reflectance spectroscopy is a tool widely used for remote sensing applications, both in planetary and terrestrial observation, as it permits the investigation of the surface mineralogy (Pieters and Englert, 1993). The ability to derive the mineralogy of planetary materials from remotely sensed reflectance spectra has been greatly improved during the last twenty years (e.g., Pieters, 1983; Smith et al., 1985; Mustard and Pieters, 1987, 1989; Sabol et al., 1992; Fischer and Pieters, 1994; Lucey et al., 1995, 1998; Sunshine and Pieters, 1998; Chabrillat et al., 2000; Shkuratov et al., 1999a; Pinet et al., 2000b).

Indeed, surfaces of most Solar System bodies are covered with a dusty regolith layer, which consists of a multicomponent mixture of various minerals and impact products. In order to better interpret the physical (texture, roughness, maturity, porosity, proportion of crystals versus fines) and mineralogical properties of the surface at subpixel scale, it is important to understand the physics that controls the light interaction process with soils components. However, this process is related to electromagnetic energy and its interaction with a particulate interface through a combination of first surface (or specular) reflection, transmission, absorption, diffraction, and multiple scattering from adjacent particles. The physics of this process is complex and, at the present time, only partially understood.

In the past years, a number of semi-empirical models have been developed for analyzing the bidirectional re-

* Corresponding author.
E-mail address: aurelien.cord@cnes.fr (A.M. Cord).

0019-1035/$ – see front matter
doi:10.1016/S0019-1035(03)00204-5

flectance data of particulate surfaces based on the scattering and absorption properties of minerals and rocks (e.g., Hapke, 1981, 1986, 1993; Johnson et al., 1992; Hiroi and Pieters, 1994; Shkuratov et al., 1999b). Using the radiative transfer equation describing the scattering of light from soils, Hapke (1993) developed an approximate analytical solution. This equation is widely used for studying reflectance data from planetary surfaces (e.g., Johnson, 1983; Helfenstein and Veverka, 1987; Cheng and Domingue, 2000). However this model is generally difficult to handle because its application relies on some assumptions of optical properties of the materials under study. It needs the knowledge of six physical parameters, linked with the multiple scattering, the phase function, the opposition effect, and the roughness. Also the complexity of Hapke's equation and the comparatively large number of model parameters (Liang and Townshend, 1996; Douté and Schmitt, 1998; Mishchenko et al., 1999; Shkuratov et al., 1999b) do not provide a unique meaningful solution (Helfenstein and Veverka, 1987).

The primary objective of the present investigation is to present a reliable method of alleviating this difficulty by solving simultaneously all the parameters involved in the Hapke's equation. It is based on a genetic algorithm and it only uses multi-angular hyperspectral images with no a priori knowledge of the material constituting the target. From experimental measurements produced by a new laboratory wide-field multispectral imaging facility (Pinet et al., 2000a, 2001) in the spectral range from 0.4 to 1.05 μm, the method is applied to three basaltic soils, each sorted to four grain sizes. An outcome is the derivation of Hapke parameters for those samples, which may be used to understand their physical meaning, in particular for the parameter θ of the function for macroscopic roughness. Their potential wavelength dependence is studied. These first results, compared with the literature, determine the success and limitations of all the steps of the approach which is taken.

After a short introduction to Hapke's model, the samples and the facility used for their measurements, we present the implementation of a genetic algorithm adapted to our problem. Then the results are analyzed.

1.1. Radiative transfer formalism

The model developed by Hapke (1993) requires the knowledge of six parameters to calculate the bidirectional reflectance (R):

$$R = \frac{w}{4(\mu_0 + \mu)}\left[\left(1 + B(g)\right)P(g) + H(\mu_0)H(\mu) - 1\right]S(\theta) \tag{1}$$

where μ_0, μ are the cosines of incidence and emergence angles, respectively, g is the phase angle, w is the single scattering albedo which depends on wavelength λ, B is the opposition effect function, P is the phase function, H is the isotropic multiple scattering function, and S is the function for macroscopic roughness.

$H(\mu)$ is the multiple scattering function. Its exact form was established by Chandrasekhar (1960), and we usually use the approximated function with a difference less than 1% exposed in Hapke (1993, p. 212). The parameter w is only needed for the calculation of H.

The double Henyey–Greenstein function, including two parameters, describes the particle phase function $P(g)$ with sufficient accuracy for most radiative transfer calculations in planetary regoliths (McGuire and Hapke, 1995; Hartman and Domingue, 1998):

$$P(g) = (1-c)\cdot\frac{1-b^2}{(1+2b\cdot\cos(g)+b^2)^{3/2}} + c\cdot\frac{1-b^2}{(1-2b\cdot\cos(g)+b^2)^{3/2}} \tag{2}$$

where b and c are the two parameters linked with the material properties and are constrained between 0 and 1: b determines the phase function form and c determines the nature of scattering ($c < 0.5$ corresponds to forward scattering and $c > 0.5$ to backward scattering).

The opposition effect is a surge in brightness observed in particulate surface near zero phase angle. This effect is described by the function $B(g)$ in Hapke's model (1993). The two parameters, h and B_0, both depend on the physical properties of the regolith. The angular width parameter h is constrained between 0 and 1 for physical reasons. It characterizes the regolith compaction and its particle size distribution law. The amplitude of the opposition effect, B_0, is an empirical parameter, with values constrained between 0 and 1. The function $B(g)$ takes into account the shadow hiding opposition effect (SHOE) only and not the coherent backscatter opposition effect (CBOE) (Hapke et al., 1998). As detailed in the following (Part 3.3), given the range of considered phase angles ($> 20°$) in this study, the CBOE should not contribute significantly (Helfenstein et al., 1997; Shepard and Arvidson, 1999; Kaasalainen et al., 2001; Shkuratov and Helfenstein, 2001).

The function for macroscopic roughness $S(\theta, \mu_0, \mu)$ is presented in Hapke (1993). The parameter θ is a mean topographic slope angle that provides a measure of surface macroscopic roughness inside a pixel. It alters the local incidence and emergence angles. S is referred to as the topographic shadowing function in the following.

1.2. Measurements

A new laboratory spectral imaging facility has been designed and installed at the Observatoire Midi-Pyrénées, Toulouse, France (Pinet et al., 2000a, 2001). It is used to obtain multispectral images of an experimental target of about 20×20 cm with varied incidence and emergence angles. Eighteen narrow band interferential filters are used for measurements in the spectral range 0.4 to 1.05 μm.

The bidirectional reflectance is obtained using a spectralon as a reference during measurements. To account for

Table 1
Angular configurations of bidirectional reflectance measurements

Incidence angle (i)	20	30	40	0	30	50	20	30	40	50
Emergence angle (e)	0	50	65	30	0	20	−35	−45	−55	−65
Phase angle (g)	20	20	25	30	30	30	55	75	95	115

its non-Lambertian behavior, the spectralon standard used has been calibrated by means of measurements produced at ONERA, Toulouse, France, and consistently compared with independent recent estimates (Bonnefoy, 2001).

The domain of geometries of observation investigated is the incidence angle selected between 0° and 55° and the emergence angle between −70° and 70° in the principal plane. The minimum phase angle is 20°. This angular domain is quite useful for carrying out laboratory experiments (Kamei and Nakamura, 2002), simulating the observational situations the most frequently encountered in planetary exploration by spaceborne optical instruments (e.g., MOC/MGS, HRSC/Mars-Express, AMIE/Smart-1, LIC/Lunar-A, LISM/Selene).

In this angular range, for deriving realistic estimates of Hapke's parameters, ten measurements are produced in order to span the photometric variability, linked with phase angle (e.g., Mustard and Pieters, 1989; McGuire and Hapke, 1995; Hillier and Buratti, 2001). The selections of angular configurations used in this work are presented in Table 1.

1.3. Sample description and preparation

We selected for this study three different materials:

- A fresh unaltered basalt, with some phenocrysts of olivine, pyroxene and plagioclase, from a lava flow of Pic d'Ysson (Massif Central, France). The general shape of the spectrum is presented in Fig. 1a. This sample is labeled "Basalt."
- A highly altered basalt, palagonitic-like material, labeled "Palagonite," from the Salagou Lake (Herault, France). This basalt has been intensively altered by low temperature water circulation (Fig. 1b).
- An oxidized basaltic red-tephra, labeled "Tephra," from Flagstaff Cinder Sales (Arizona, USA) containing few phenocrysts of plagioclase. This material is related to explosive-type basaltic volcanism, with some effects of iron oxidation (Fig. 1c).

The chosen materials present different spectral properties (Fig. 1): one is a grey material with no spectral dependence (basalt) while the two others have a high reflectance increase as a function of wavelength.

Their chemical whole rock analyses are given in Table 2.

Materials were crushed to produce powders having grain size less than 3 mm and were sorted into four classes using sieves. The grain size for each class is the following: less than 75 µm (labeled "G1"), from 75 to 250 µm ("G2"), from 250 to 500 µm ("G3"), and from 500 µm to 2 mm ("G4").

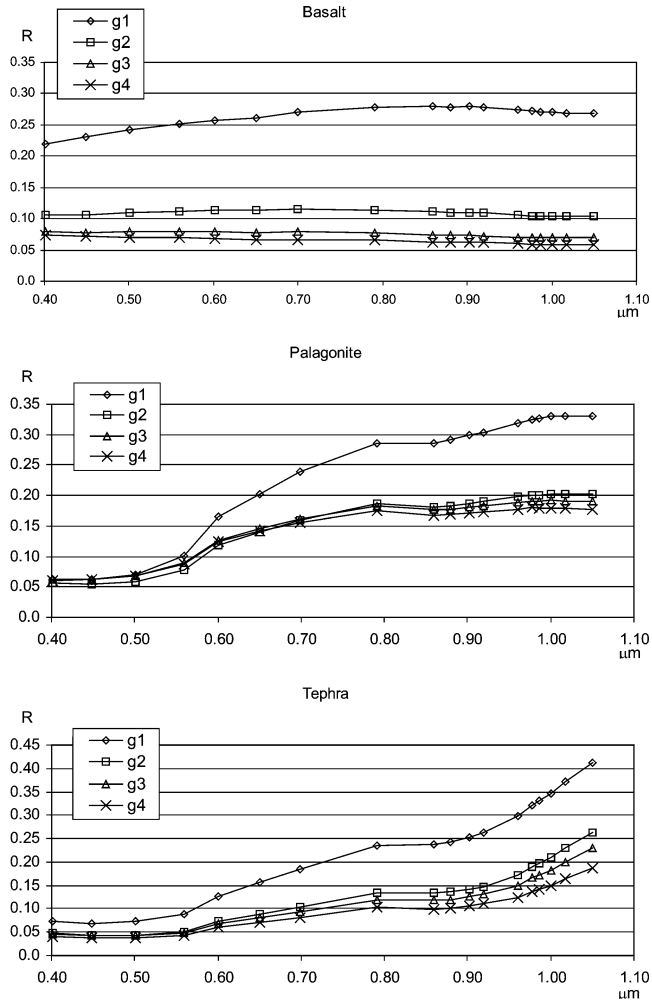

Fig. 1. Bidirectional reflectance spectra (R) for the three materials and for all grain size classes. Incidence angle is 30° and emergence −45°.

As a result, we used twelve samples (the three materials with four different classes of grain size) in order to explore the intermediate domain of the parametric space both in terms of grain size and level of reflectance typical of planetary rocky surfaces, particularly in the case of Mars. A natural extension of this study would be to measure also bright icy materials and very low albedo materials.

A target composed of the twelve samples is used for measurement (Fig. 2). When preparing the target, the powders are poured into the sample dishes and gently tapped to induce settling. Consequently each surface is flattened and all significant macroscopic topography effects are eliminated.

Table 2
Chemical whole rock analyses for the three materials (weight %). Precision on determination is ±1%

	SiO_2	Al_2O_3	Fe_2O_3	MnO	MgO	CaO	Na_2O	K_2O	TiO_2	P_2O_5	LOI
Basalt	42.8	11.5	12.9	0.3	15.3	9.6	2.7	1.2	2.1	0.6	1.0
Palagonite	45.8	19.4	7.3	0.1	3.2	5.4	2.2	4.1	0.6	0.2	11.7
Tephra	48.0	17.9	11.8	0.2	5.8	9.7	3.7	0.7	1.7	0.5	0.2

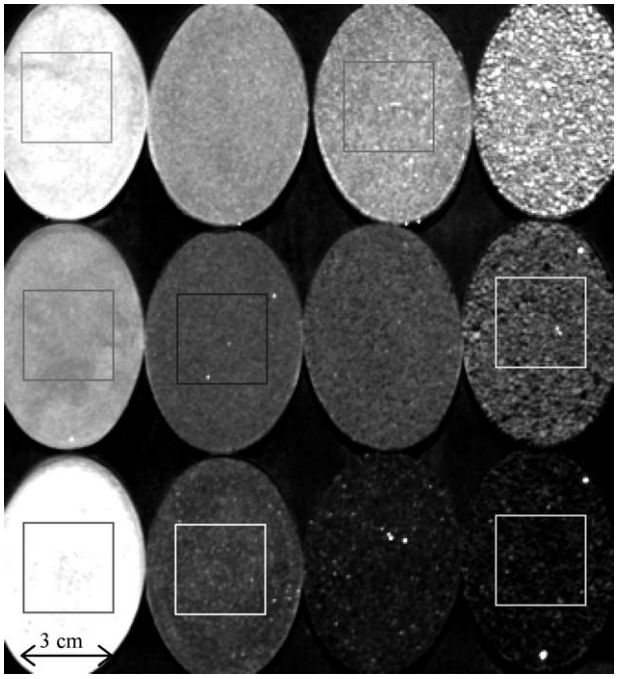

Fig. 2. Target composed of three materials for the different classes of grain size. In each column, from top to bottom: Palagonite, Tephra, and Basalt samples, in the first one the grain size is less than 75 μm (G1), in the second column grain sizes are from 75 to 250 μm (G2), in the third grain sizes are from 250 to 500 μm (G3) and in the fourth grain sizes are from 500 μm to 2 mm (G4). The squares are examples of macroscopic cell in which measurements are averaged.

The Fig. 3 shows photomicrographs of samples having grain sizes classes G1 and G4 with a magnification of 100. It illustrates that grains are mainly clumps of aggregated small particles, coexisting with individual beads.

In the following, we will consider three levels of scale:

- A microscale level that describes the particulate medium having typical size about ten times the wavelength (until a few tens of microns). The smallest grain size class samples (G1) are mainly composed of such small particles.
- A macroscale level representing the underlying large topography variations of the samples. Given the sample preparation mentioned above, this macroscopic topography is controlled and has no influence in this study.
- A mesoscale level that is intermediate between these two scales: it depends on the surface boundary topography (referred to in the following as the textural topography) with features in the submillimetric-centimetric range and is dominated by the "rocky" aspect of the surface involving the shape, roughness and topographic structure of grains (in particular for the G3 and G4 grain size classes).

The Fig. 3 shows that at the scale of a few tens of microns the roughness of the grains is the same whatever the sample prepared from a given material, showing that the microscale properties remain similar.

For each sample, we simultaneously record many independent measurements (about 150 × 180 pixels) at a sampling of 200 μm per pixel. This experimental technique simulates better the case of planetary regolith, where the optical properties are influenced by the physical variability related to the surface texture. With this type of measurements, the contribution of optical effects associated with anisotropic surfaces may be increased, requiring a better handling in the photometric modeling (e.g., Hapke, 2002). Then we extract, from the data, the spectrum of each sample, averaging within a given macroscopic cell of three by three centimeters, the measured values for each wavelength (Fig. 2). This contrasts with the usual experimental data produced by integrated spot measurements.

2. Genetic algorithms

The objective of this study is to model, using radiative transfer equations, reflectance spectra for the twelve samples describe above. For each of them, we have 10 spectra, resulting from the angular configurations (Table 1), made of 18 discrete wavelength measurements. It implies the determination, without any a priori assumptions, of the Hapke parameters that fit at best the measurements, minimizing the difference between the measured and modeled spectra (Cord et al., 2002a). Considering a large number of data, a genetic algorithm is chosen; the principal advantages in applying this technique are:

- all Hapke's parameters are treated simultaneously with no a priori additional assumptions, thus limiting the risk of meeting a local extreme,
- all the configurations have the same weight, i.e., all available data are used to solve the problem,
- as an improvement to Monte Carlo method (Hillier and Buratti, 2001), the genetic algorithm is optimizing calculation time.

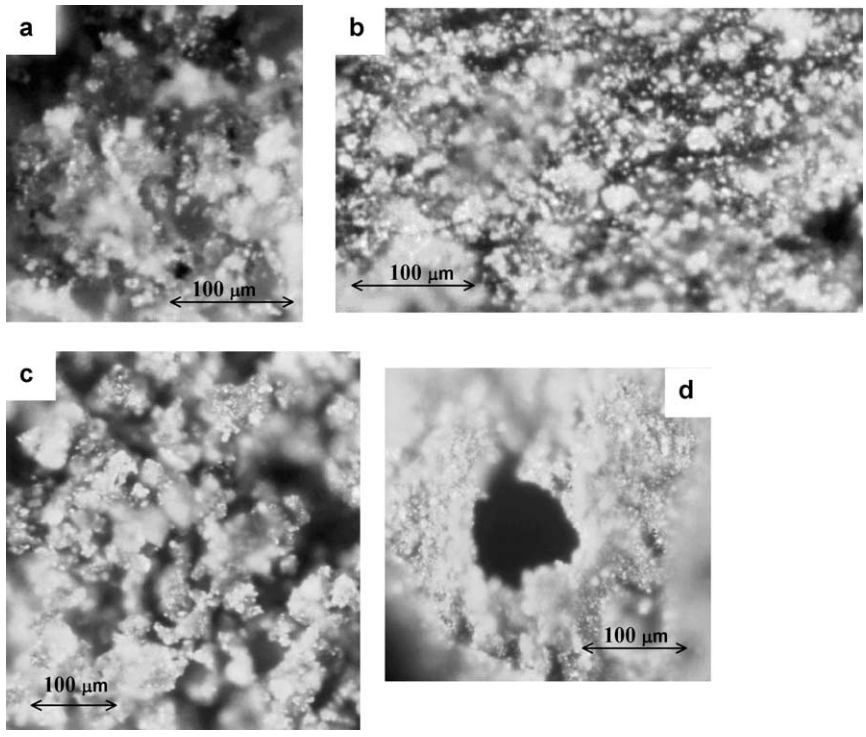

Fig. 3. Photomicrographs (reflected light) of: (a) Basalt G1 (×100), (b) Basalt G4 (×100), (c) Tephra G1 (×100), (d) Tephra G4 (×100).

Genetic algorithms are a part of evolutionary computing, which is a rapidly growing area of artificial intelligence, invented by John Holland in 1975 (Holland, 1975). They are inspired by Darwin's evolution theory.

The algorithm starts with a set of randomly generated suitable solutions (represented by chromosomes) called a population. Evaluating their score estimates, the best chromosomes are selected to become parents: they cross over and mutate to form new offspring (children). In this way, a new population, having the same size as the original one is formed, expecting that it will have some better score estimates than the previous one. This is repeated until some given conditions are satisfied.

The outline of the basic genetic algorithm is very general and its implementation to determine Hapke's parameters requires us to address some issues: how are the chromosomes created and what type of encoding is best suited to this problem? Encoding, crossover and mutation adapted to the present problem are presented in the following section.

2.1. Chromosome encoding

In the present case, we use a "direct encoding" method (Goldberg, 1989) where a chromosome corresponds to a sequence of Hapke's parameters: it consists in a string composed of six genes: five real values (b, c, h, B_0, θ) plus one spectrum $w(\lambda)$. Thus, a chromosome contains all the information required to model spectra in bidirectional reflectance as a function of incidence and emergence angles. We search for the best chromosome allowing the model to fit measured spectra.

2.2. Population generation

The search space is defined by means of the physical limits allowed by the equation of radiative transfer (Hapke, 1993): b, c, B_0, and h are constrained between 0 and 1 as described above. Compiling the values found for the parameter θ in the case of non-icy planetary bodies (Table 11), we notice that it is always between 0° and 40°.

To generate an initial chromosome, each of the five first genes (b, c, h, B_0, θ) is randomly determined in this search space. Then, using these parameters and Hapke's equation, the single scattering albedo spectrum $w(\lambda)$ is optimized, minimizing the difference between measured and modeled spectra.

Population size is given by the number of chromosomes (in one generation) and depends mainly on the encoding method. On one hand, if the population is too small, the genetic algorithm will converge too quickly to a local optimal point and may not be able to find the best solution. On the other hand, if there are too many chromosomes, it results in a long computing time with no significant improvement for the solution (Goldberg, 1989). In our case, it can be shown that an initial population of 10,000 chromosomes gives good results (see section: convergence and repeatability).

2.3. Fitness or score

This optimized determination of the difference between observed and modeled reflectance spectra is controlled using a criterion of score estimates: we define the absolute score as the mean of absolute difference between measured and

modeled spectra for all wavelengths and all angular configurations (Eq. (3)). Its value is minimized.

$$\textit{Absolute\_Score} = \frac{\sum\sum_{\substack{configurations,\\ wavelengths}} |Spectrum_{measured} - Spectrum_{modelled}|}{Nb_{configurations} \times Nb_{wavelengths}}. \quad (3)$$

2.4. Parent chromosomes selection

The next step is the selection of the 10,000 parents for crossover.

The parent chromosome selection is easier to understand when we have a fitness score to maximize; consequently in the following part, we consider as a criterion the inverse of the absolute score defined above.

We want to select the better parents, expecting that they will produce the better offspring. Also the first idea is that the probability of reproduction directly depends on the score estimate of each chromosome. However the use of this method can lead to two kinds of problems: First, if a very efficient subject is too often selected, the whole population tends to converge towards its genome. The diversity of the new offspring is then too much reduced to allow the genetic algorithm to progress further. Second, with the progression of the genetic algorithm, the differences between fitness decrease. In that case the best ones have similar selection probabilities to the others and the genetic algorithm cannot improve the result anymore. In order to avoid these problems, the fitness value is transformed and a windowing is applied. For each chromosome, the fitness is reduced by the fitness of the worst chromosome. This permits us to strengthen the strongest subject and to obtain a zero based distribution. Thus the probability of reproduction directly depends on this new value.

Subsequently the method, which is applied, is the following: Considering S_i, the inverse of absolute score of the ith chromosome:

1. A new fitness score S' is calculated:
$$S'_i = \frac{S_i - \min(S_i)}{\text{mean}(S_i - \min(S_i))}. \quad (4)$$
2. The integer part of it E_i is determined and the ith chromosome is selected E_i times (a chromosome having a fitness score less than the mean is not selected at this step).
3. To end the selection, lacking parents are selected proportionally to the decimal part of S'.

For instance, a chromosome with S' equal to 2.6 is selected twice during the step 2, and has the same probability to be selected in the step 3 as a chromosome having a score of 0.6.

2.5. Crossover

In genetic algorithms, the crossover rate must be high, about 80 to 95% (Goldberg, 1989). In our case, a rate chosen between 80 and 95% has a negligible influence on the results. We take a value of 80%. Crossover between two parents consists of a random exchange of the five first genes (b, c, h, B_0, θ). Two parent chromosomes generate two offspring chromosomes. An example of crossover is presented in Table 3.

2.6. Mutation

After crossover is performed, mutation takes place. It changes randomly the new offspring. This prevents all solutions of the solved problem, given a population, from falling into a local optimum. Mutation rate is generally very low in genetic algorithms, about 0.5 to 1% (Goldberg, 1989), because if it occurs very often, the genetic algorithm results in a random search, such as in the case of a Monte Carlo algorithm. In our case, a mutation rate chosen between 0.5 and 1% has negligible influence on results. We take a value of 1%. When mutation takes place to produce an offspring chromosome, one of the five first genes (b, c, h, B_0, θ) is replaced by a random value. An example of mutation is presented in Table 4.

2.7. Elitism

It is possible that making a new population only by new offsprings results in the loss of the best chromosome in the last population. To avoid this, an artifact called elitism is used. This means that at least the best solution can be copied without change to a new population, so it survives to the last run.

Table 3
Example of crossover

Parent 1	Parent 2	CROSSOVER	Offspring 1	Offspring 2
b1	b2	→	b1	b2
c1	**c2**	⇒	**c2**	**c1**
h1	**h2**	⇒	**h2**	**h1**
$B_0$1	$B_0$2	→	$B_0$1	$B_0$2
θ1	**θ2**	⇒	**θ2**	**θ1**

Parents 1 and 2 are reproduced together (changing parameters are in bold).

Table 4
Example of mutation

Offspring 1	MUTATION	Offspring 1′
b1	→	b1
c2	⇒	**c0**
h2	→	h2
$B_0$1	→	$B_0$1
θ2	→	θ2

Offspring 1 (defined in Table 3) is mutated on the gene c (in bold).

Table 5
Repeatability of genetic algorithm

	SCORE	b	c	h	B_0	θ	w (nm)		
							559	791	1001
MEAN	0.006	0.41	0.52	0.33	0.13	19.2	0.31	0.60	0.76
STDDEV	0.000024	0.007	0.014	0.046	0.018	0.20	0.0031	0.0029	0.0028

Mean and standard deviation of Hapke parameters determination when the processing has been run six times for the Tephra G2 samples. The score value is the absolute score calculated for this sample.

2.8. Loop

For each chromosome of the new offspring population, an optimized single scattering albedo spectrum (w) is calculated, minimizing the difference between measured and modeled spectra with Hapke's equation using the first five genes as parameters. It gives a new complete population and the process is reiterated from the fitness evaluation until the population score estimate is no more improving.

2.9. Convergence and repeatability

After about 40 iterations, the genetic algorithm converges and there is no additional improvement of the results as the iterative process goes further.

To check the repeatability, the processing has been carried out six times for one of the twelve samples (Tephra G2), with initial populations being randomly chosen (Table 5). From these independent runs, the variations of results are not the same for all parameters, but for a given parameter they remain much smaller than its confidence estimate (defined and determined in the following). This method shows that:

- A unique solution to the problem exists rather than several solutions giving equivalent results.
- The genetic algorithm converges to the solution.
- The population size is large enough to solve the problem.

Comparing this algorithm with a Monte Carlo method having the same precision, we evaluate that the genetic algorithm is about 20,000 times more efficient. The longest part of the process during the inversion is to find the optimized determination of the single scattering albedo for each chromosome. The number of determinations calculated is about 0.5×10^6 for the genetic algorithm (10,000 chromosomes, 50 iterations). For comparison, in the Monte Carlo method, if we consider 100 values for each of the 5 parameters, the number of determinations is $100^5 = 10{,}000 \times 10^6$. On a SUN Fire 6800 under Solaris 8, the typical computational time for determining the full set of Hapke parameters, using the genetic algorithm, is less than one hour for a given sample.

The genetic algorithm is therefore a powerful tool, providing a global determination of the set of Hapke's parameters from a suite of angular configurations.

3. Results

In this section, after a calculation of an estimate on the accuracy for the parameter determination, the results of the optimized resolution of the global set of Hapke's parameters are analyzed for the samples under consideration.

3.1. Fitness

Despite the fact that the geometries of observation are in the principal plane and that their number is limited, the fitness between model and data is a non-trivial one: As a matter of fact, for each sample, we have 10 geometries of observation with 18 wavelengths, i.e., 180 measurements. Under the assumption that Hapke's parameters (except w) are not wavelength-dependent at the first order (this hypothesis will be tested in the following), the model has 5 wavelength-independent parameters (b, c, B_0, h, θ) and one spectrum $w(\lambda)$ of 18 wavelengths, i.e., 23 free parameters.

As an example, we display in Fig. 4 the measured and modeled bidirectional reflectance spectra for the tephra G3 sample. In Figs. 4a and 4b, we notice that the model nicely reproduces the spectral variations associated with angular configurations and in Fig. 4c, it is shown as a function of the phase angle for the wavelength 0.601 µm. The difference between measured and modeled reflectance spectra, assessed using the absolute score estimate (Eq. (3)), is listed in Table 6 for all of the samples. Knowing that the estimated accuracy on the measurements with the instrument is from 0.005 to 0.01 in reflectance (Pinet et al., 2000a), the optimized score fitness must be of the same order or slightly less. Indeed, the residuals in reflectance associated with the absolute score estimate range between 0.003 and 0.01 for all samples. These values, which are on the order of or less than the measurement uncertainty estimate, show that with the determined parameters, Hapke's model is able to reproduce variations in spectral features due to incidence and emergence angles for the different materials considered here. To check the precision of the inversion for each parameter, we

Table 6
Absolute score estimate for each sample $\times 10^2$

	G1	G2	G3	G4
Basalt	1.04	0.65	0.81	0.83
Palagonite	0.59	0.65	0.66	0.63
Tephra	0.50	0.46	0.65	0.34

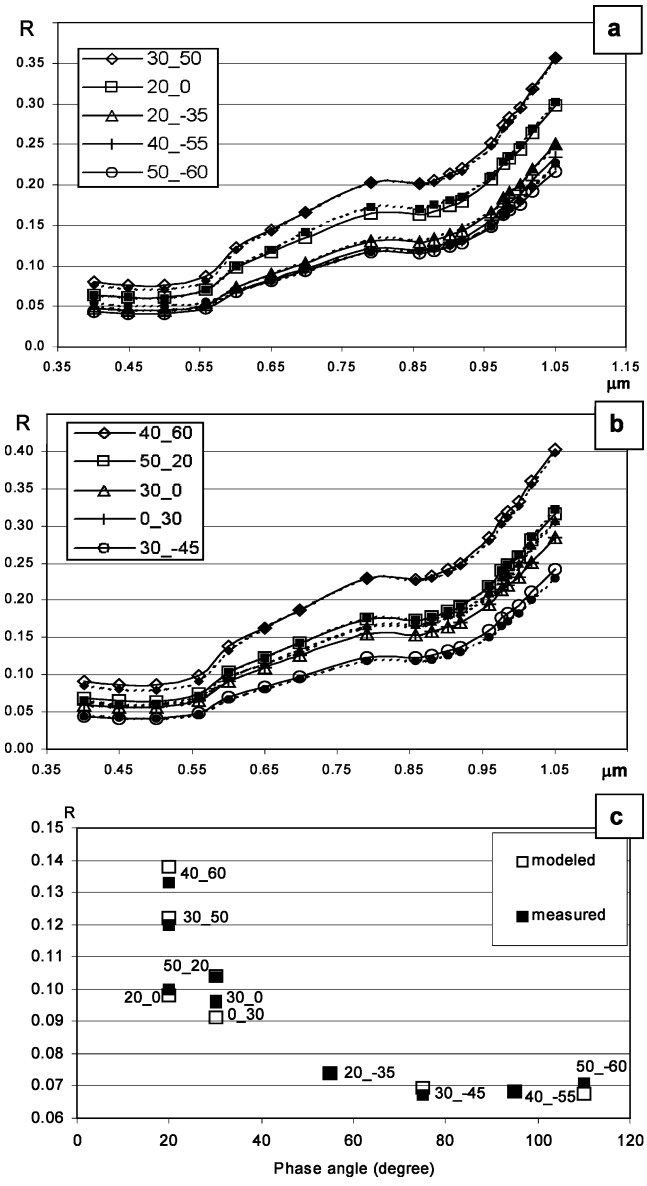

Fig. 4. Measured and modeled bidirectional reflectance spectra (R) of the Tephra G3 sample, for the 10 configurations of observation: (a), (b) as a function of wavelength. The dotted lines are the measured spectra and solid lines are modeled spectra; (c) as a function of phase angle for wavelength of 0.601 µm. The filled squares are the measured values and the transparent squares the modeled values. In the key, the first number corresponds to the incidence angle and the second number to the emergence angle.

calculate score estimate variations versus parameter variation (δ).

$$\textit{Score\_estimate\_variation}(\delta) = \frac{\textit{Score}(\text{opt}+\delta) - \textit{Score}(\text{opt})}{\textit{Score}(\text{opt})}. \quad (5)$$

The curves of score variation (Fig. 5) reveal that the determinations of optimal values for each parameter are generally well constrained and that all the parameters are not evaluated with the same precision.

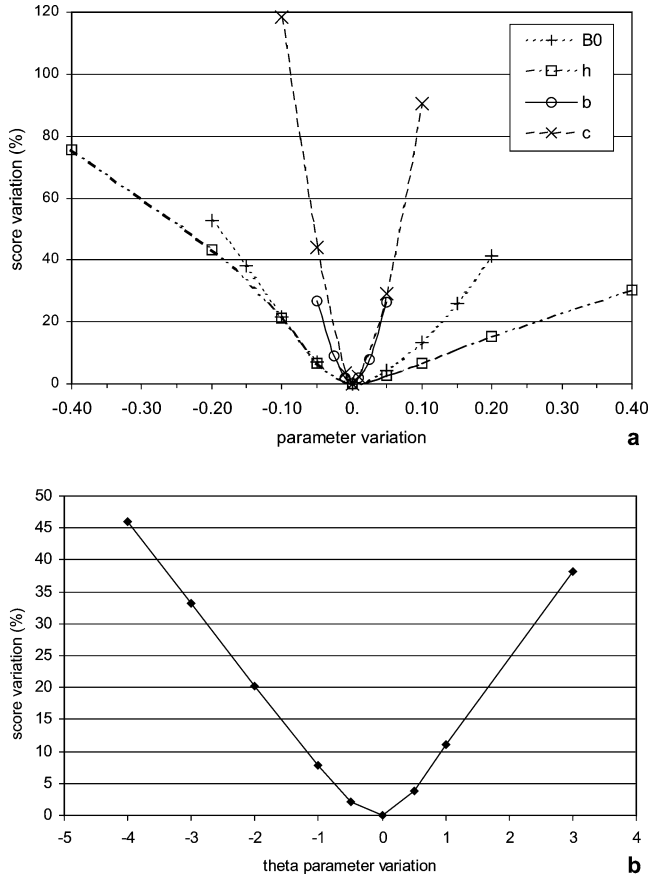

Fig. 5. Score variation versus parameter variation: (a) for B_0, h, b, and c; (b) for θ.

To assess the repeatability and the stability expected on each parameter determination, ten runs with nine out of the ten angle configurations (Table 1) were performed for the samples related with the smallest and largest parameter values (Basalt G1, Palagonite G3, and Tephra G4). The mean results of those runs are presented in Table 7 together with the results of the run using the ten angle configurations for all parameters. On the basis of these calculations, an estimate on the accuracy for the parameters determination is derived from the standard deviations: the uncertainties are ± 0.03 for b and c, $\pm 1°$ for θ, and ± 0.1 for B_0 and h. The value of the h parameter for the Basalt G1 sample does not influence the score, due to the low amplitude of the opposition effect. Therefore, to constrain this parameter, only the Palagonite G3 and Tephra G4 samples results are considered.

Even with the limited set of angular configurations, we can constrained Hapke's model and estimate the accuracy for each parameter. An increase of the number of viewing angles could allow us to improve precision on the estimation of parameters; in particular, with phase angles smaller than 20° we could better constrain the determination of the opposition effect function parameters.

To study the wavelength dependence, independent determinations of parameter values for five wavelengths selected along the spectral domain (0.603, 0.783, 0.901, 0.974,

Table 7
For the three samples Basalt G1, Palagonite G3, and Tephra G4, Hapke's parameter values calculated

Basalt G1	b	c	B_0	h	θ
Value—10 conf.	0.49	0.13	0.15	0.24	5.8
Mean—9 conf.	0.51	0.11	0.14	0.28	5.8
Std dev.—9 conf.	0.021	0.010	0.062	0.202	0.87
Spectral Std dev.	0.003	0.009	0.031	0.033	0.74
Palagonite G3					
Result—10 conf.	0.44	0.40	0.39	0.18	21.9
Mean—9 conf.	0.45	0.42	0.38	0.19	21.2
Std dev.—9 conf.	0.030	0.028	0.050	0.073	0.75
Spectral Std dev.	0.014	0.048	0.084	0.044	0.514
Tephra G4					
Result–10 conf.	0.41	0.56	0.64	0.58	28.7
Mean—9 conf.	0.43	0.52	0.56	0.59	30.7
Std dev.—9 conf.	0.010	0.027	0.044	0.061	0.80
Spectral Std dev.	0.009	0.047	0.058	0.051	1.16

During the run using all the angular configurations (line 1) and during runs using nine of the ten angular configurations (mean on line 2, standard deviation on line 3). During these runs, the average of standard deviations of parameter values for different wavelengths are determined (on line 4).

1.02 µm) are calculated (Table 7). We first notice a second order variation for some parameters (c, θ) (cf. Fig. 7) (Cord et al., 2003a).

Considering the fitness estimate and the accuracy of measurements determined, the parameter values are analyzed in the following: we compare them with those found elsewhere (e.g., Mustard and Pieters, 1989; McEwen, 1991; McGuire and Hapke, 1995; Shepard and Campbell, 1998; Clark et al., 2002; Domingue et al., 2002), we study their potential wavelength dependence and we investigate the links between values and grain sizes.

3.2. *Phase function* (b, c)

Values of phase function parameters (b, c) derived from the genetic algorithm are presented in Table 8, with an uncertainty in the determination about ± 0.03.

We first note that b values, linked with the form of the phase function, remain between 0.4 and 0.5 for all the samples. While the three sample materials have very different spectral behaviors, the b parameter is semi-constant, suggesting that b may have similar values when one considers different planetary surfaces.

Table 8
Values of phase function parameters (b, c)

b	G1	G2	G3	G4
Basalt	0.49	0.45	0.41	0.39
Palagonite	0.48	0.44	0.44	0.45
Tephra	0.47	0.41	0.40	0.41
c				
Basalt	0.13	0.30	0.32	0.42
Palagonite	0.24	0.42	0.40	0.39
Tephra	0.30	0.52	0.52	0.56

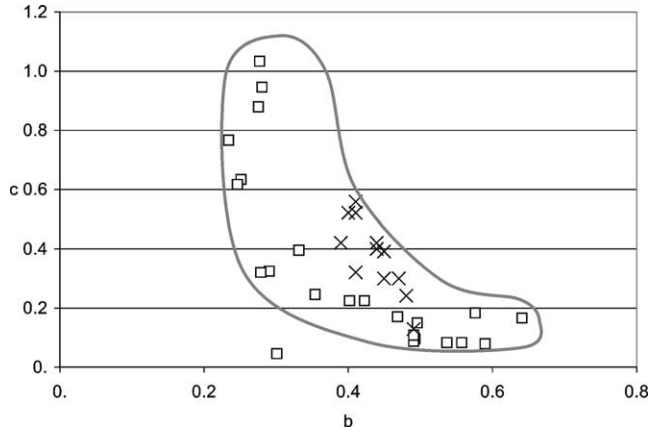

Fig. 6. Comparison between our values (crosses) of phase function parameters and those found by McGuire and Hapke, 1995 (squares).

Only the c parameter, linked with the back or forward scattering, varies with samples: c ranges from 0.13 to 0.56 and generally increases with grain size. For small grain sizes, the grains are fine enough to allow a light ray to pass through them, resulting in forward scattering, whereas larger grain sizes lead to backward scattering.

McGuire and Hapke (1995) conducted an experimental study, which gave some phase function parameters for large irregular spheres (approximately 1 cm diameter) for three kinds of materials (glass, metal and polyester resin) having different surface roughness. We compare, in Fig. 6, our results with this study: it displays a plot of b versus c values. Phase function values given by the genetic algorithm are close to values determined by Mcguire and Hapke for rough surfaced dielectric spheres or spheres with a low density of internal scatterers. Our planetary material analogs are not spheres but the phase functions are quite similar. It may come from the roughness of grains at the microscale (cf. Fig. 3) that is comparable to that of the rough surfaced spheres and from the presence of internal scatterers in our samples.

Figures 7a and 7b show the wavelength dependence for the phase function parameters. The b parameter remains almost constant in our range of wavelengths; the variations are on the order of the confidence estimate we have established and show no specific trend. For Palagonite and Tephra, the c parameter shows a weak but systematic increase as a function of wavelength. On the contrary, for basalt, it decreases from 0.125 to 0.105 (Fig. 1b). These second order effects expose a relative variation in the contribution of backward scattering versus forward scattering.

3.3. *Opposition effect function* (B_0, h)

From Hapke et al. (1998), the lunar opposition effect appears to be the result of a narrow CBOE peak with a half width of about 2° superimposed on a much broader SHOE peak about 8° wide. Helfenstein et al. (1997) give similar values from analysis of a different lunar data set: the Moon's

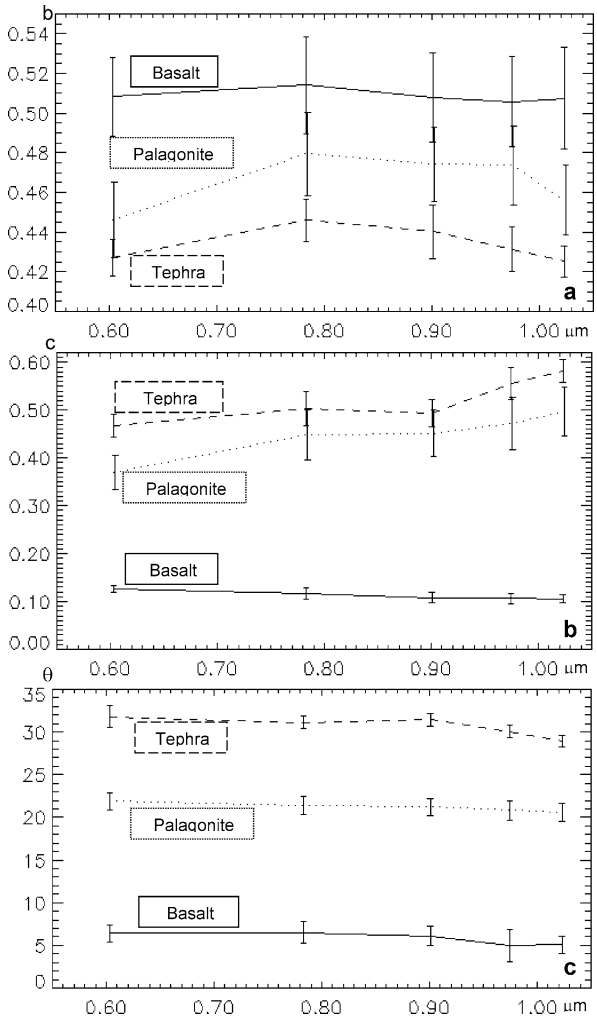

Fig. 7. Wavelength dependence of the Hapke parameters. (a) for b phase function parameters, (b) for c phase function parameter, (c) for the shadowing function parameter θ. The solid line corresponds to the Basalt G1 sample, the dotted line to the Palagonite G3 sample and the dashed line to the Tephra G4 sample.

opposition surge is well represented by a narrow CBOE peak whose effect is most strongly defined at a phase angle less than 2° combined with a very broad SHOE peak best defined over a phase angle less than 20°. In this study, we do not span the full phase angle domain; in particular, as mentioned earlier, all phase angles are greater than 20°. Consequently, only SHOE should influence the measurements. In a future study, it is intended to address CBOE producing low phase angles measurements.

Under the present conditions, values of opposition effect function parameters derived from the genetic algorithm are presented in Table 9 with a rather large uncertainty on the order of ±0.1 and one may consider that these parameters are poorly constrained. So from those parameters neither interpretative results are derived nor a wavelength dependence study is carried out.

Table 9
Values of opposition effect function parameters (B_0, h)

B_0	G1	G2	G3	G4
Basalt	0.15	0.13	0.16	0.18
Palagonite	0.00	0.25	0.39	0.59
Tephra	0.00	0.13	0.35	0.64
h				
Basalt	0.24	0.14	0.14	0.24
Palagonite	0.00	0.13	0.18	0.11
Tephra	0.00	0.33	0.54	0.58

3.4. Topographic shadowing function (θ)

Table 10 presents values of the topographic shadowing function parameter θ derived from the genetic algorithm with an uncertainty on the determination of about ±1°. We first note that θ values are highly correlated with grain sizes of the samples: 14° for g1, 20° for g2, 23° for g3, and 26° for g4 in the case of bright materials such as palagonite or tephra; 6° for g1, 13° for g2, 16° for g3, 21° for g4 in the case of a darker material such as basalt.

We show in Fig. 7c a 10 to 15% decrease of the topographic shadowing function parameter as the wavelength increases. This second order variation confirms the assumption of Shepard and Campbell (1998), that shadows may differ for the same surface at different wavelengths. A hypothesis is that when the albedo increases with the wavelength, then primary shadowed areas are partly illuminated from multiple scattered photons, leading to an underestimation of θ.

In Hapke's theory, the θ parameter, referred to as the surface roughness, takes into account the effects due to the shadowing inside each pixel and to the local changing of the incident and emission angles. θ is considered by Hapke (1993) to represent the mean slope angle averaged over all distances on the surface between upper and lower limits that are determined by the resolution of the detector and the physics of radiative transfer equation. Shepard and Campbell (1998) suggest that the smallest faceted scale is the dominant scale for surface shadowing, but that it is not the only one to contribute to shadows on a surface. Helfenstein and Shepard (1999) found, for typical lunar regolith surfaces, that θ estimates range between 24° and 27° and that the relative contribution from surface relief at scales of 8 cm and larger is small in comparison to the contribution from surface relief at submillimeter scale.

For the smallest grain size class (G1), we may consider that the target is mainly composed of a particulate medium (microscale). The θ values, between 5.8° and 14.4° (Ta-

Table 10
Values of the topographic shadowing function parameter (θ)

θ	G1	G2	G3	G4
Basalt	5.8	13.5	16.2	20.7
Palagonite	14.4	20.4	21.9	24.9
Tephra	14.2	19.2	23.6	28.7

Table 11
Single scattering albedo (w) and topographic shadowing function parameter (θ) at ~ 0.5 μm for non icy planetary bodies

Object	w	θ (°)	Source
Almalthea	0.09 ± 0.2	13 ± 8	Simonelli et al. (2000)
Ariel	0.65	27	Skypeck et al. (1991)
Average S-asteroids	0.23[a]	20	Helfenstein and Veverka (1989)
Callisto, leading side	0.43[a]	36	Buratti (1989)
Callisto, trailing side	0.45[a]	29	Buratti (1989)
Dactyl	0.21 ± 0.03	23 ± 5	Helfenstein et al. (1996)
Eros	0.42 ± 0.01[a]	24 ± 2	Clark et al. (2002)
Gaspra	0.36 ± 0.07[a]	29 ± 2	Helfenstein et al. (1994)
Ida	0.22 ± 0.02	18 ± 2	Helfenstein et al. (1994)
Mathilde	0.035	19	Clark et al. (1999)
Mercury	0.2	16 ± 1	Mallama et al. (2002)
Metis	0.12 ± 0.03	28 ± 10	Simonelli et al. (2000)
Moon disk integrated	0.21	20	Helfenstein and Veverka (1987)
Moon, dark terrain	0.16 ± 0.03	24 ± 1	Helfenstein and Shepard (1999)
Moon, average terrain	0.31 ± 0.03[a]	26 ± 1	Helfenstein and Shepard (1999)
Moon, bright terrain	0.40 ± 0.03[a]	27 ± 1	Helfenstein and Shepard (1999)
Oberon	0.35[a]	20	Buratti et al. (1990)
Thebe	0.06 ± 0.02	17 ± 10	Simonelli et al. (2000)
Titania	0.5[a]	25	Buratti et al. (1990)
Umbriel	0.25[a]	18	Buratti et al. (1990)

[a] Indicates single scattering albedo data derived from telescopic and orbital observations, in the range of our laboratory measurements produced with G3–G4 classes.

ble 10), are principally related with the microscale features (shape and roughness of particles). On the basis of these new laboratory measurements, we agree with Shepard and Campbell (1998) and Helfenstein and Shepard (1999) that even for fine particles the contribution of θ is not negligible and that particulate samples used in laboratory measurements cannot be assumed to be photometrically smooth (i.e., $\theta = 0°$).

In the case of larger grain sizes, in the millimeter range (G3, G4), the θ parameter increases by 10° or 15°, depending on the material. In this case, the microscale properties remain similar to the G1 case (cf. Fig. 3), but the textural topography variation inside the pixels is dominated by the "rocky" aspect of the surface coming from the grains, sizing between 250 μm and 2 mm, and defining in the millimetric-centimetric range what we call the mesoscale properties (Cord et al., 2002b, 2003b). The impact of their slope and distribution on the mesoscale topographic structure inside a pixel has a large influence on the topographic shadowing function.

In the last decade, integrated telescopic and spaceborne photometric observation has progressively evolved from whole-disk toward disk-resolved measurements at regional scales (e.g., Buratti et al., 1990; Helfenstein et al., 1994; De Grenier and Pinet, 1995; Simonelli et al., 2000; Clark et al., 2002). We compare, in Table 11, our results with the compilation of θ parameter values for the case of regolithic ice-free soils derived from those observations. The search space for this parameter ranged between 0 and 40°; the present determination for the investigated materials is found to be between 5° and 30°. Both the single scattering albedo at 0.559 μm (Table 12) and the θ estimates derived for G3 and G4 classes are very much within the range of the values resulting from photometric observations at regional scale. It appears that the most representative case for describing the photometric behavior of natural regolith surfaces lies in the G3–G4 texture classes. The values derived from planetary measurements may be controlled by the contribution of coarse-grained materials on the surface, not necessarily involving a high macroscopic roughness with large surface slopes at the hundred meters scale as it is often suggested. We affirm that the main effect that influences the topographic shadowing function results predominantly from a combination of the microscale and mesoscale characteristics. It involves the shape, roughness and topographic structure of grains smaller than the centimeter, these grains being either clumps of aggregated small particles or individual beads and shards. Therefore the contribution from scales larger than the centimeter is almost negligible. On this experimental basis, we confirm Helfenstein and Shepard (1999), that the parameter θ is mainly an integral of the roughness properties in the submillimetric—centimetric range inside the pixel of observation.

Shepard and Campbell (1998) suggest that a surface roughness parameter extracted photometrically should have values not only depending on the surface properties, but also on the observed material nature. Based on the present θ determinations, we strengthen the case that the θ quantity depends on both the grain size and the material geological properties.

3.5. Single scattering albedo

An example of single scattering albedo spectra is plotted on Fig. 8 for the Palagonite. Values of the single scattering albedo at 0.559 μm derived from the genetic algorithm are presented in Table 12. In comparison with Table 11, we note

Table 12
Modeled single scattering albedo (w) at 0.559 μm

	G1	G2	G3	G4
Basalt	0.82	0.57	0.45	0.40
Palagonite	0.56	0.45	0.48	0.48
Tephra	0.51	0.32	0.29	0.25

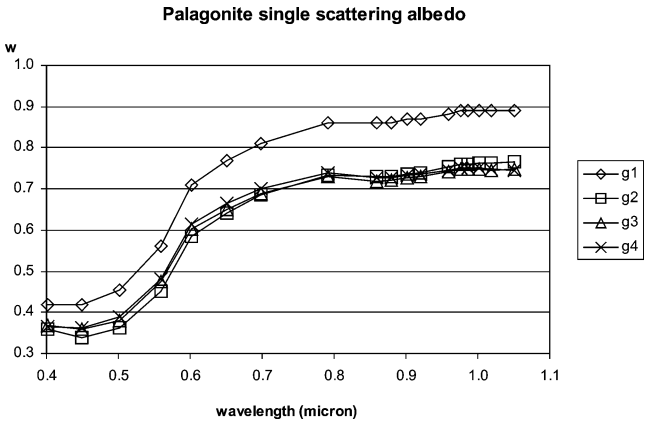

Fig. 8. Single scattering spectra of Palagonite samples for all grain size classes.

that large grain size samples (G3, G4) have similar photometric properties to non icy planetary materials, as detailed above.

The physical properties described by the single scattering albedo relate to regolith composition (e.g., Helfenstein, 1988; Hapke, 1993). In this study, the inversion using Hapke's model results in a single scattering albedo higher for G1, as shown in the Fig. 8 in the case of Palagonite. For the smallest particles, the G1 photometric properties are very different to those of larger classes and do not fit those of non-icy planetary bodies (Table 11). Though we agree with previous studies (e.g., Pieters and Englert, 1993; Pieters et al., 1993; Mustard and Hays, 1997) demonstrating the spectroscopic importance of the fine fraction in the optical behavior of the lunar soils, our present results based on an experimental photometric approach show that natural regolith surfaces observed at regional scale, differently from the case of laboratory sample powders, are likely not composed of fine grain size materials only; however, among the coarse-grained materials constituting the natural regolith, the possibility exists that a significant proportion of aggregates or clumps of small particles be present.

3.6. Discussion

The Hapke's formalism, using the parameter values determined by the genetic algorithm, models well the variations in bidirectional reflectance related to particle grain size distribution for the three materials. We first establish an estimate on the accuracy for the parameters determination: ± 0.03 for b and c, $\pm 1°$ for θ, and ± 0.1 for B_0 and h, indicating that phase function and topographic shadowing function parameters are well constrained. This shows that the angular domain available in this study (phase angle between 20° and 120°) is large enough to determine the phase function. However, the opposition effect function and roughness parameters are less constrained. To better describe opposition effect, smaller phase angle measurements are needed. A complementary study is planned to measure the same samples with low phase angles in the range 0°–20°.

Furthermore a by-product of this application is the derivation of Hapke parameters for samples having grain sizes and levels of reflectance typical of planetary rocky surfaces; it may be used in future reflectance spectroscopy data interpretations, particularly in the case of Mars. We found that:

- b retains similar values for all samples, between 0.4 and 0.5.
- c generally increases with grain size and albedo, showing that both large grains and high albedo materials lead to a prevailing backward scattering and that small grains and dark materials lead to forward scattering.
- θ values are highly correlated with grain sizes of the samples: 14° for g1, 20° for g2, 23° for g3, and 26° for g4 in the case of bright materials; 6° for g1, 13° for g2, 16° for g3, 21° for g4 in the case of a darker material such as basalt.

Additionally, we study the wavelength dependence of parameters for five different wavelengths:

- b remains almost constant along all the spectral range of investigation.
- c value decreases slightly with the wavelength for dark material and increases for light materials.
- θ decreases very slowly when increasing the wavelength.

These results strengthen the case that the implicit assumption that Hapke's parameters are constant with wavelength is not totally valid. Indeed, it would be worth extending this preliminary exploration toward the infrared. Our results also highlight the need for an improved interpretation of this dependence.

In addition, the methods presented can be easily generalized and applied:

- To test different models of radiative transfer, assessing whether or not the fit is better for alternative models. In particular, it will be very interesting to use the upgraded Hapke's formalism (Hapke, 2002) taking into account anisotropic multiple scattering.
- To investigate the case of samples such as natural rock surfaces and bulk soils rather than powder, to simulate different textural situations representative of planetary surface states.

- To better define the angular conditions under which orbital observations must be conducted to access to the local photometric function of planetary surfaces.

4. Conclusion

The method used in this study, based on a genetic algorithm, gives access to an optimized determination of the global set of Hapke's parameters, for planetary analog surfaces when dealing with experimental multi-angular spectro-imaging data. The results validate all the steps along the methodology implemented, including experimental measurements and the derivation of Hapke's model photometric quantities using the genetic algorithm.

In fact this kind of study is required to improve interpretation techniques in preparation for upcoming remote sensing data at high spatial resolution and/or under varied geometries (Mars Express, SMART1, LUNAR-A). The objective, when interpreting data from these platforms will be to quantify the mineralogy of planetary materials at sub-pixel scale. An established method to solve this problem is to apply a spectral linear mixing on the single scattering albedo spectra (Johnson, 1983). If these spectra are evaluated using Hapke's equation, one needs a determination of all parameters. The present work allows the study of the optical characteristics of analogs of non-icy planetary surfaces versus grain sizes and material composition. in order to improve the understanding and the physical meaning of Hapke's parameters, in particular of the shadowing function parameter (θ). It appears that the microscale and mesoscale textural features less than the centimeter scale contribute predominantly to the photometric effect related to the rocky aspect of planetary soil surfaces. The parameter θ may thus be mainly considered as an integral of the mesoscale and micro-scale roughness properties in the submillimetric-centimetric range. The most representative case for describing natural regolith surface is represented by texture classes in the millimeter range, not necessarily involving a high macroscopic roughness with large surface slopes at the hundred meter scale.

These results highlight the need for an improved theoretical modeling, incorporating a potential second-order spectral dependence of the photometric parameters, to describe the real case of natural regolithic surfaces, for which the photometric behavior is influenced by the mesoscale organization of the textural relief.

Acknowledgments

This work has been supported by the French Programme National de Planétologie/INSU/CNRS, the French Space Agency CNES, the Paul Sabatier University of Toulouse and INTAS grant 2000-0792. We also acknowledge the technical support of Observatoire Midi-Pyrénées and of Lasoptic Company for the implementation and the operation of the wide field spectral imaging facility. We gratefully thank the two anonymous reviewers for their constructive and thorough comments, which substantially improved this paper. We are deeply indebted to Esther Harris for her painstaking corrections of this manuscript.

References

Bonnefoy, N., 2001. Développement d'un spectrophoto-goniomètre pour l'étude de la reflectance bidirectionnelle des surfaces géophysiques. Application au soufre et perspective pour Io. Thesis. Laboratoire de Glaciologie et Géophysique, Univesité Joseph Fourier, Grenoble I.

Buratti, B.J., 1989. Callisto: new evidence for a hemispheric difference in surface texture. Bull Am. Astron. Soc. 21, 983–984.

Buratti, B.J., Wong, F., Mosher, J., 1990. Surface properties and photometry of uranian satellites. Icarus 84, 203–214.

Chabrillat, S., Pinet, P.C., Ceuleneer, G., Johnson, P.E., Mustard, J.F., 2000. Ronda peridotite massif: methodology for its geological mapping and lithological discrimination from airborne hyperspectral data. Int. J. Remote Sens. 21 (12), 2363–2388.

Chandrasekhar, S., 1960. Radiative Transfer. Dover, New York.

Cheng, A.F., Domingue, D.L., 2000. Radiative transfer models for light scattering from planetary surfaces. J. Geophys. Res. 105 (E4), 9477–9482.

Clark, B.E., Helfenstein, P., Bell III, J.F., Veverka, J., Izenberg, N.I., Domingue, D., Wellnitz, D., McFadden, L.A., 2002. NEAR infrared spectrometer photometry of Asteroid 433 Eros. Icarus 155, 189–204.

Clark, B.E., Veverka, J., Helfenstein, P., Thomas, P.C., Bell III, J.F., Harch, A., Robinson, M.S., Murchie, S.L., McFadden, L.A., Chapman, C.R., 1999. NEAR photometry of Asteroid 253 Mathilde. Icarus 140, 53–65.

Cord, A.M., Pinet, P.C., Daydou, Y., Chevrel, S., 2002a. Determination of Hapke's equation parameters using multiangular bidirectional reflectance spectra. In: E.G.S., 27th, p. 1304.

Cord, A.M., Pinet, P.C., Daydou, Y., Stankevich, D., Shkuratov, Yu., 2002b. Planetary regolith surface analogs and mesoscale topography: optimized determination of Hapke parameters using multi-angular spectro-imaging laboratory data. In: Solar System Remote Sensing, 2002, pp. 17–18. Abstract.

Cord, A.M., Pinet, P.C., Daydou, Y., Chevrel, S., 2003a. Experimental investigation of the potential wavelength dependence of Hapke parameters in the visible and near infrared range. In: Proc. Lunar Planet. Sci. Conf. 34th. Abstract #1548, Houston.

Cord, A.M., Pinet, P.C., Daydou, Y., Chevrel, S., 2003b. Experimental determination of the Hapke shadowing function parameter for planetary regolith surface analogs. In: Proc. Lunar Planet. Sci. Conf. 34th. Abstract #1349, Houston.

De Grenier, Pinet, P., 1995. Near-opposition martian limb-darkening: quantification and implication for visible-near infrared bidirectional reflectance studies. Icarus 115, 354–368.

Domingue, D., Robinson, M.S., Carcish, B., Joseph, J., Thomas, P.C., Clark, B.E., 2002. Disk-integrated photometry of 433 Eros. Icarus 155, 205–219.

Douté, S., Schmitt, B., 1998. A Multilayer bidirectional reflectance model for the analysis of planetary surface hyperspectral images at visible and near-infrared wavelengths. J. Geophys. Res. 103 (E13), 31367–31389.

Fischer, E.M., Pieters, C.M., 1994. Remote determination of exposure degree and iron concentration of lunar soils using VIS-NIR spectroscopic method. Icarus 111, 475–488.

Goldberg, D.E., 1989. Genetic Algorithms in Search, Optimization and Machine Learning. Addison–Wesley.

Hapke, B., 1981. Bidirectional reflectance spectroscopy. 1. Theory. J. Geophys. Res. 86 (B4), 3039–3054.

Hapke, B., 1986. Bidirectional reflectance spectroscopy. 4. The extinction coefficient and the opposition effect. Icarus 67, 264–280.

Hapke, B.W., 1993. Theory of reflectance and Emittance Spectroscopy. Cambridge Univ. Press, New York.

Hapke, B., 2002. Bidirectional reflectance spectroscopy. 5. The coherent backscatter opposition effect and anisotropic scattering. Icarus 157, 523–534.

Hapke, B., Nelson, R., Smythe, W., 1998. The opposition effect of the moon: coherent backscatter and shadow hiding. Icarus 133, 89–97.

Hartman, B., Domingue, D., 1998. Scattering of light by individual particles and the implications for models of planetary surfaces. Icarus 131, 421–448.

Helfenstein, P., 1988. The geological interpretation of photometric surface roughness. Icarus 73, 462–481.

Helfenstein, P., Shepard, M., 1999. Submillimeter-scale topography of the lunar regolith. Icarus 141, 107–131.

Helfenstein, P., Veverka, J., 1987. Photometric properties of lunar terrains derived from Hapke's equation. Icarus 72, 342–357.

Helfenstein, P., Veverka, J., 1989. Physical characterization of asteroid surfaces from photometric analysis. In: Binzel, R., Gehrels, T., Matthews, M.S. (Eds.), Asteroids II. Univ. of Arizona Press, Tucson, pp. 557–593.

Helfenstein, P., Veverka, J., Hillier, J., 1997. The lunar opposition effect: test of alternative models. Icarus 128, 2–14.

Helfenstein, P., Veverka, J., Thomas, P.C., Simonelli, D.P., Klaasen, K., Johnson, T.V., Fanale, F., Granahan, J., McEwen, A.S., Belton, M., Chapman, C.R., 1996. Galileo photometry of Asteroid 243 Ida. Icarus 120, 48–65.

Helfenstein, P., Veverka, J., Thomas, P.C., Simonelli, D.P., Lee, P., Klaasen, K., Johnson, T.V., Breneman, H., Head, J., Murchie, S.L., Fanale, F., Robinson, M.S., Clark, B.E., Granahan, J., Garbeil, H., McEwen, A.S., Kirk, R., Davies, M., Neukum, G., Mottola, S., Wagner, R., Belton, M., Chapman, C.R., Pilcher, C., 1994. Galileo photometry of Asteroid 951 Gaspra. Icarus 107, 37–60.

Hillier, J.K., Buratti, B.J., 2001. Monte Carlo simulations of light scattering by composite particles in planetary surface. Icarus 149, 251–261.

Hiroi, T., Pieters, C.M., 1994. Estimation of grain sizes and mixing ratios of fine powder mixtures of common geologic minerals. J. Geophys. Res. 99 (E5), 10867–10879.

Holland, J.H., 1975. Adaptation in Natural and Artificial System. Univ. of Michigan Press, Ann Arbor.

Johnson, P.E., 1983. A semiempirical method for analysis of the reflectance spectra of binary mineral mixtures. J. Geophys. Res. 88 (B4), 3557–3561.

Johnson, P.E., Smith, M.O., Adams, J.B., 1992. Single algorithms for remote determination of mineral abundances and particle size from reflectance spectra. J. Geophys. Res. 97 (E2), 2649–2657.

Kaasalainen, S., Piironen, J., Muinonen, K., 2001. Opposition effect of regolith-type materials. In: E.G.S. 26th. Abstract.

Kamei, A., Nakamura, A.M., 2002. Laboratory study of bidirectional reflectance of powdered surfaces: on the asymmetry parameter of asteroid photometric data. Icarus 156, 551–561.

Liang, S., Townshend, J.R.G., 1996. A modified Hapke model for soil bidirectional reflectance. Remote Sens. Environ. 55, 1–10.

Lucey, P.G., Blewett, D.T., Hawke, B.R., 1998. Mapping the FeO and TiO2 content of the lunar surface with multispectral imagery. J. Geophys. Res. 103 (E2), 3679–3699.

Lucey, P.G., Taylor, G.J., Malaret, E., 1995. Abundance and distribution of iron on the Moon. Science 268, 1150–1153.

Mallama, A., Wang, D., Howard, R.A., 2002. Photometry of Mercury from SOHO/LASCO and Earth. Icarus 155, 253–264.

McEwen, A.S., 1991. Photometric functions for photoclinometry and other applications. Icarus 92, 298–311.

McGuire, A.F., Hapke, B., 1995. An Experimental study of light scattering by large, irregular particles. Icarus 113, 134–155.

Mishchenko, M.I., Dlugach, J.M., Yanovitskij, E.G., Zakharova, N.T., 1999. Bidirectional reflectance of flat, optically thick particulate layers: an efficient radiative transfer solution and applications to snow and soil surfaces. J. Quant. Spectrosc. Rad. 63, 409–432.

Mustard, J., Hays, J., 1997. Effects of Hyperfine particles on reflectance spectra from 0.3 to 25 microns. Icarus 125, 145–163.

Mustard, J.F., Pieters, C.M., 1987. Quantitative abundance estimates from bidirectional reflectance measurements. Proc. Lunar Planet. Sci. Conf. 17th, Part 2. J. Geophys. Res. 92 (B4), E617–E626.

Mustard, J.F., Pieters, C.M., 1989. Photometric phase functions of common geologic minerals and applications to quantitative analysis of mineral mixture reflectance spectra. J. Geophys. Res. 94 (B10), 13619–13634.

Pieters, C.M., 1983. Strength of mineral absorption features in the transmitted component of near-infrared reflected light: first results from RELAB. J. Geophys. Res. 88 (B11), 9534–9544.

Pieters, C.M., Englert, P.A.J., 1993. Remote Geochemical Analyses: Elemental and Mineralogical Composition. Cambridge Univ. Press, New York.

Pieters, C.M., Fischer, E.M., Rode, O., Basu, A., 1993. Optical effects of space weathering: the role of the finest fraction. J. Geophys. Res. 98, 20817–20824.

Pinet, P.C., Boubault, F., Daydou, Y., Chevrel, S., 2000a. Implementation of a laboratory wide field spectral imaging facility. In: E.G.S. 25th. Abstract.

Pinet, P.C., Shevchenko, V.V., Chevrel, S.D., Daydou, Y., Rosemberg, C., 2000b. Local and regional lunar regolith characteristics at Reiner Gamma Formation: optical and spectroscopic properties from Clementine and Earth-based data. J. Geophys. Res. 105 (E4), 9457–9475.

Pinet, P.C., Cord, A., Daydou, Y., Boubault, F., Chevrel, S., Lapeyrere, V., 2001. Influence of linear versus non-linear mixture on bidirectional reflectance spectra using a laboratory wide field spectral imaging facility. In: Proc. Lunar Planet. Sci. Conf. 32nd, p. 1552. Abstract.

Sabol Jr., D.E., Adams, J.B., Smith, M.O., 1992. Quantitative subpixel spectral detection of targets in multispectral images. J. Geophys. Res. 97 (E2), 2659–2672.

Shepard, M.K., Arvidson, R.E., 1999. The opposition surge and photopolarimetry of fresh and coated basalts. Icarus 141, 172–178.

Shepard, M.K., Campbell, B.A., 1998. Shadows on a planetary surface and implications for photometric roughness. Icarus 134, 279–291.

Shkuratov, Yu., Helfenstein, P., 2001. The opposition effect and the quasi-fractal structure of regolith: I. Theory. Icarus 152, 96–116.

Shkuratov, Yu.G., Kaydasch, V.G., Opanasenko, N., 1999a. Iron and titanium abundance and maturity degree distribution on lunar nearside. Icarus 137, 222–234.

Shkuratov, Yu., Starukhina, L., Hoffman, H., Arnold, G., 1999b. A model of spectral albedo of particulate surfaces: implications for optical properties of the moon. Icarus 137, 235–246.

Simonelli, D.P., Rossier, Laura, Thomas, P.C., Veverka, J., Burns, J.A., Belton, M.J.S., 2000. Leading/trailing albedo asymmetries of Thebe, Amalthea, and Metis. Icarus 147, 353–365.

Skypeck, A., Veverka, J., Helfenstein, P., Baker, L., 1991. The photometric roughness of Ariel is not unusual. Icarus 90, 181–183.

Smith, M.O., Johnson, P.E., Adams, J.B., 1985. Quantitative determination of mineral types and abundances from reflectance spectra using principal components analysis. Proc. Lunar Planet. Sci. Conf. 15th. J. Geophys. Res. 90 (Suppl.), C797–C804.

Sunshine, J.M., Pieters, C.M., 1998. Determining the composition of olivine from reflectance spectroscopy. J. Geophys. Res. 103 (E6), 13675–13688.